Task 5: Improvements to WRF Representation of Residual Layer

AQRP Project 24-021

Improving WRF representation of coastal, marine, and residual boundary layers and quantifying the effects on ozone prediction

Prepared by

Yuxuan Wang, University of Houston

James Flynn, University of Houston

April 15, 2025

1. Introduction

In our previous Task 4, we focused on improving marine planetary boundary layer height (PBLH) by identifying the optimal physics schemes and parameterizations within the Weather Research and Forecasting (WRF) v4.6.0 baseline configuration. We performed numerous simulations, evaluated the results, and selected the 3 best-performing configurations, PBLH5, PBLH12, and PBLH14, which improved PBLH prediction over water. These selected perturbation runs also resolved some of the major issues in the baseline configurations, such as 'cloud-like' features in PBLH distribution and unrealistically high nighttime PBLH over urban Houston. Apart from the 3 best-selected perturbation simulations from Task 4, we continued our efforts to explore additional parameters and schemes to enhance the model simulations of PBLH over water. Details will be discussed in Section 4 of this report.

In Task 5, our focus shifted to improving the representation of the residual layer (RL) in the WRF model. The WRF base configuration exhibits a notable gap in representing the RL height, as it only estimates the stable and convective boundary layers while omitting the elevated residual structure (Liu et al., 2023). In this task, first, we developed an empirical method to diagnose the RL height from the WRF base model using the vertical gradient of potential temperature ($\partial\theta/\partial z$) and verified these diagnosed RL with available observational datasets. Second, for the three best-performing perturbation simulations from Task 4, along with the new sensitivity runs, we evaluated the model-predicted PBLH against observations. Lastly, we applied the developed empirical method to calculate RL height across the entire simulation domain for both the WRF base model and the selected perturbation simulations to evaluate the changes in RL from the perturbation simulations.

2. Model configuration and case day selection

This section contains information about the base model configuration in the WRF and selected case days. This information has already been discussed in the Task 4 report and is included here for the reader's convenience.

2.1. Base model configuration

The Weather Research and Forecasting (WRF) model version 4.6.0 with the Advanced Research WRF (ARW) solver was employed to simulate meteorological fields for three domains (**Figure 1)** over the contiguous United States (d01 - 12km×12km), Southeast Texas (d02 - 4km×4km), and the Houston-Galveston region (d03 - 1.33km×1.33km), respectively. All three domains have identical vertical resolutions with 30 vertical levels from the surface to ~100 hPa. As the base WRF configurations, we used the local closure Mellor-Yamada-Nakanishi-Niino Level 2.5 (MYNN2) PBL scheme (Nakanishi & Niino, 2009), Morrison double moment (2M) microphysics scheme (Morrison et al., 2009), Rapid Radiative Transfer Model (RRTMG)

longwave and shortwave radiation schemes (Iacono et al., 2008), Monin-Obukhov similarity surface layer scheme (Chen et al., 1997), Noah land-surface module (Chen & Dudhia, 2001), and the New Tiedtke cumulus parameterization (Tiedtke, 1989; Zhang et al., 2011). The initial and boundary conditions (IC/BC) for domain d01 were derived from the High-Resolution Rapid Refresh (HRRR) model, while the IC/BC for d02 were generated from d01, and those for d03 were generated from d02. These configurations were selected from our previous work that yielded the best prediction of overall meteorological conditions (Liu et al., 2023) during the Tracking Aerosol Convection ExpeRiment-Air Quality (TRACER-AQ) field campaign period that took place from July – October 2021(TAQ1) (Jensen et al., 2021). In the present study, we expanded the evaluation by incorporating observational data from all three TRACER-AQ field campaigns: TAQ1 (July to October 2021), TAQ2 (April to October 2022), and TAQ3 (May to October 2023). The red lines in domain d03 (**Figure 1**) represent the mobile platform sampling tracks from these campaigns.

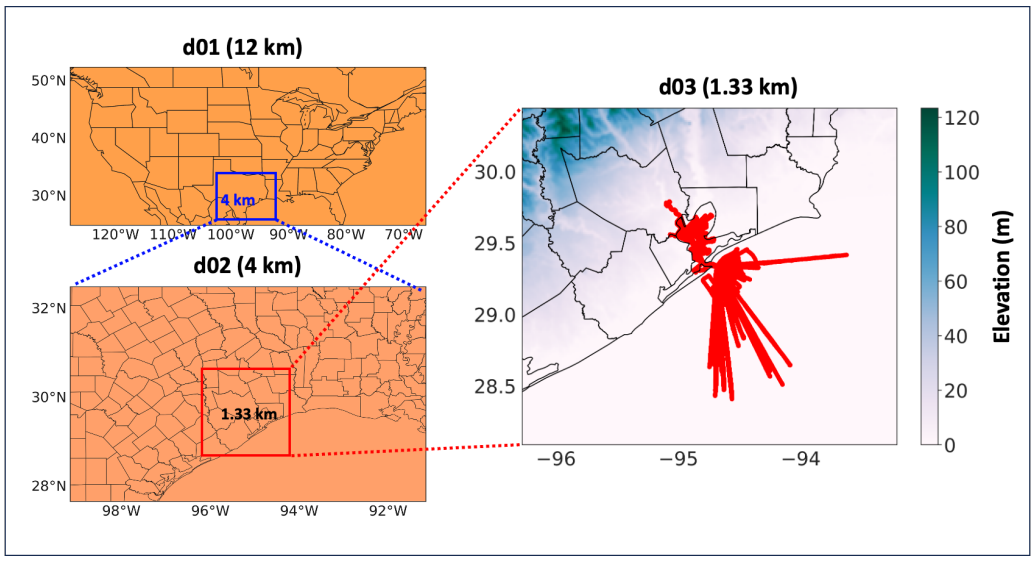

Figure 1 WRF domains showing d01 (contiguous United States), d02 (Southeast Texas), and d03 (Houston-Galveston) regions. Red lines in d03 are the locations of ship-based measurements from University of Houston Pontoon Boat (UHPB), Red Eagle boat (RE), and Osprey Boat (OB).

2.2. Selected days for model perturbation

The selected days for the model perturbation are based on the model evaluation in Task 3, as well as our previous modeling analysis of TAQ1 and TAQ2 campaign datasets. A total of 9 days were chosen for model perturbation/sensitivity simulations: July 27-28, September 09, and September 24-26, 2021; September 08-10, 2022; and May 19 and September 09 - 10, 2023. The selection criteria for these dates consider multiple factors, including various locations in Galveston Bay and the Gulf of America, both near and far from land, including the Houston Ship

Channel (HSC). Other criteria include different times of day, varying pollutant levels, and the availability of both mobile and stationary observational data. These diverse factors help ensure a comprehensive evaluation of the model. Figure 2 shows the locations for each selected day with the time of day for each observation point.

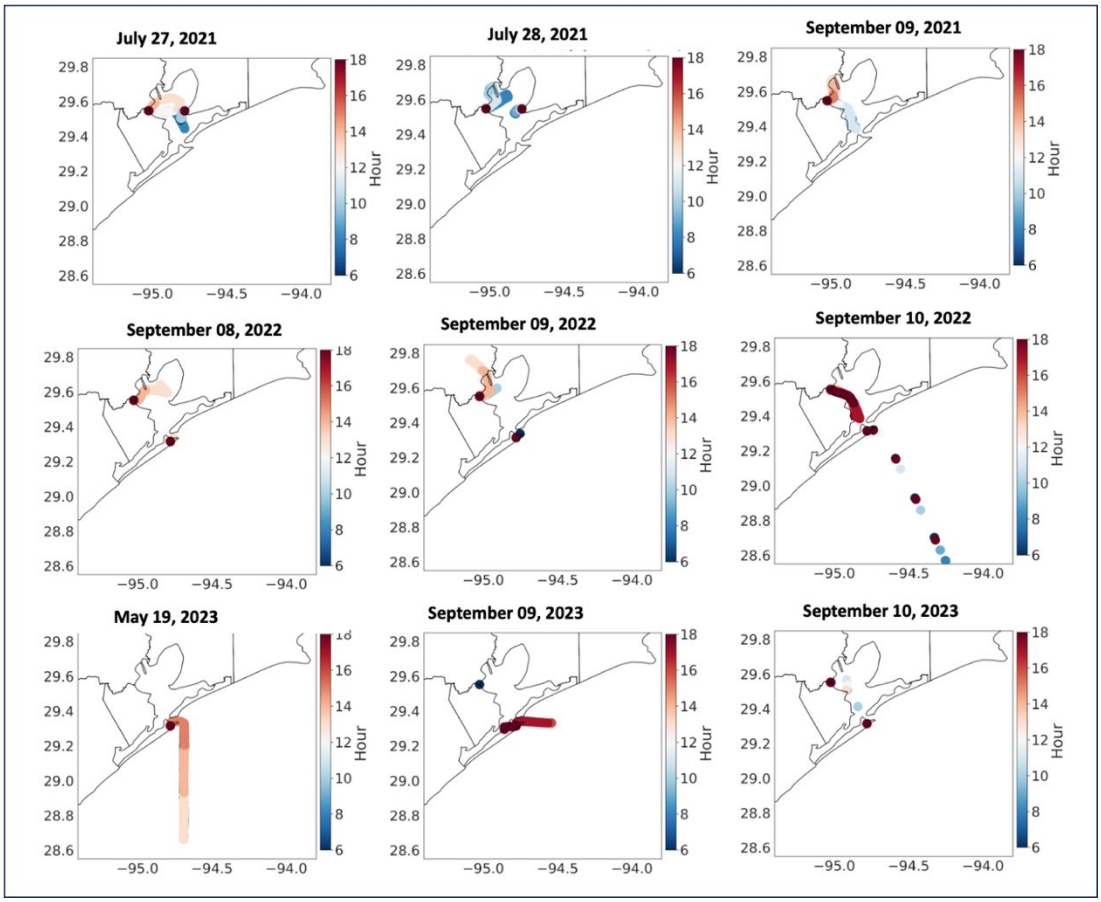

Figure 2 Location of the selected days for model perturbation. Color in the spatial map represents the time of observation.

3. Residual layer Diagnosis

The planetary boundary layer (PBL), typically extending up to ~2 km, is the lowest part of the troposphere directly influenced by surface forcings. During the day, surface heating generates turbulence, forming a convective boundary layer (CBL) characterized by vertical mixing. After sunset, turbulence decays and the CBL transitions into a residual layer (RL) aloft (~1–2 km) while the surface layer cools and forms a shallow, stable boundary layer (SBL) below (~0–0.5 km). From our previous work (Liu et al., 2023) which analyzed PBL variations in the Houston region during September 2021 period, we observed that the diurnal structure of daytime CBL followed by nighttime SBL is typically dominant under less polluted or low-ozone conditions. However, during high-ozone episodes in the Houston area, a RL was found to persist overnight.

This persistence of RL was often capped by a strong capping inversion (CI). The elevated RL can trap pollutants aloft and potentially contribute to next-day ozone buildup.

In the WRF base model, only a single-layer PBL height is diagnosed. The model identifies only the shallow SBL at night and fails to capture the overlying residual layer (Liu et al., 2023). To address this limitation, we developed an empirical method, described below, to diagnose the residual layer height using the vertical gradient of potential temperature ($\partial\theta/\partial z$) which is capable of identifying strong capping inversions and layered thermal structures within the model.

3.1. Thermodynamic calculation of residual layer

To diagnose the residual layer, we first analyzed vertical profiles of the potential temperature gradient ($\partial\theta/\partial z$) from the WRF base model at LaPorte for September 2021. The LaPorte site was selected due to the availability of continuous, stationary ceilometer-observed PBLH observations throughout the month, which allowed for abundant datapoints to develop the empirical method based on comparing the modeled thermodynamic structure with observed boundary layer features. Our previous work (Liu et al., 2023) showed that the LaPorte ceilometer observations clearly identified the presence of a stable boundary layer (SBL) on clean-air days and a well-defined residual layer (RL) on high-ozone days. By comparing the modeled $\partial\theta/\partial z$ profiles with these observed structures, we found that the model reproduced sharp vertical gradients in potential temperature that corresponded well with the observed RL heights. The observed agreement provided confidence in developing an empirical-based approach to diagnose the RL height by analyzing the thermodynamic structure in the model.

On comparing observed PBL and modeled $\partial\theta/\partial z$, we found that strong temperature inversions associated with the top of the RL typically occurred where $\partial\theta/\partial z$ exceeded 6.6 °C/km at LaPorte. This threshold was applied in our empirical algorithm to identify temperature inversion layers within the model as follows. At each model grid column in time and space, the algorithm searched for the strongest thermal inversion defined as a continuous sequence of at least three vertical levels where $\partial\theta/\partial z$ exceeded 6.6 °C/km; the search was limited to heights below 3 km above the surface. The height at which this sharp inversion occurred (the first point in the three consequent thermal inversion layers) was then recorded as the residual layer height. If no strong inversion was found, the algorithm then searched for weaker but still meaningful gradients using lower thresholds of 3.0, 2.0, and 1.0 °C/km, each requiring at least four continuous vertical levels exceeding these thresholds. The search first happens with a threshold of 3.0 °C/km and moves to a lower threshold if no residual layer assessment is made for the given threshold. These additional thresholds allowed the method to capture more diffuse or less well-defined boundary layer structures, especially under transitional or weakly stable conditions.

There could still be some limited days, e.g., clean days, where none of the gradient thresholds will be met. To still have a PBL assessment for these days, which will associate with boundary layer height, the algorithm identifies a boundary layer by checking for any noticeable increase in potential temperature with height. Specifically, it searched for the first level where $\partial\theta/\partial z$

exceeded 3.0, 2.0, or 1.0 °C/km. Once such a value was found, the corresponding height was recorded as the estimated boundary layer height. Using those smaller thresholds, this method is able to identifying shallow surface-based stable boundary layer (SBL) associated with nocturnal radiative cooling.

The combined approach with sharp inversion identification or the identification of noticeable increase in $\partial\theta/\partial z$ allowed us to diagnose different boundary layer structures, including the stable boundary layer (SBL), the convective boundary layer (CBL), and the residual layer (RL). On clean-air days, the diurnal cycle is typically characterized by a shallow SBL at night and a well-developed CBL during the day. In contrast, under polluted conditions, a persistent residual layer capped by a strong inversion often forms overnight.

Figure 3 shows example plots comparing the thermodynamically diagnosed residual layer (RL) height (green markers) based on the vertical gradient of potential temperature ($\partial\theta/\partial z$), observed PBLH from the ceilometer (red markers), base model-predicted PBLH (black line) for September 2 and September 24, 2021, at LaPorte. The background contour represents the modeled $\partial\theta/\partial z$ profile, which highlights key atmospheric structures, such as capping inversions. On September 2, no strong capping inversion was observed, and both the observations and model indicate a relatively shallow boundary layer throughout the day. In contrast, on September 24, a distinct capping inversion is present, and the ceilometer data clearly shows the existence of a nocturnal residual layer. While the WRF base model fails to capture this structure by simulating only a shallow stable boundary layer at night, the diagnosed RL height from the potential temperature gradient closely matches the observed RL. This demonstrates the utility of the diagnostic approach for identifying residual layers that are otherwise missing in the model output. In the afternoon, the diagnosed layer (green markers) is comparable to model-derived PBLH, which is an indirect verification of our method of thermodynamically-diagnosed RL.

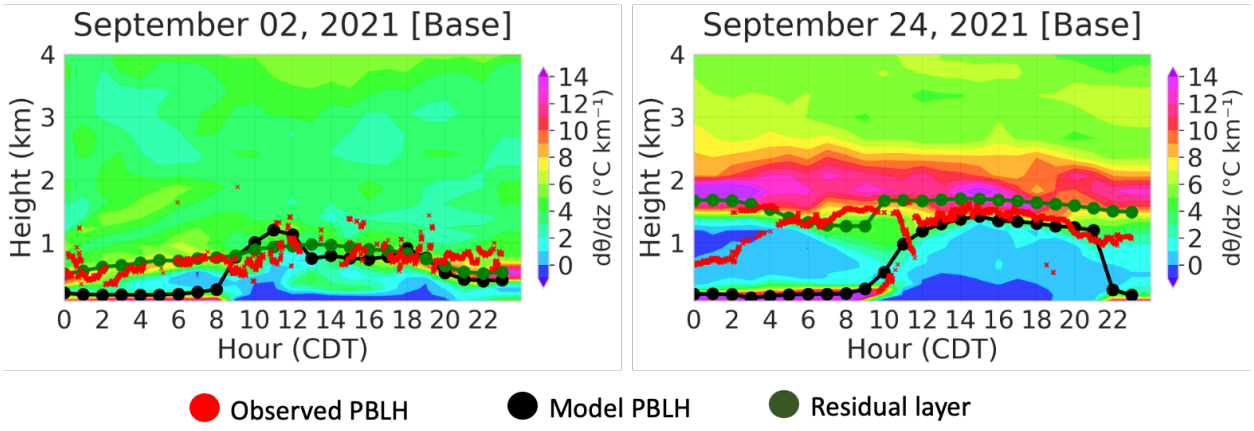

Figure 3 Thermodynamically identified residual layer (RL), along with the observed and base modeled planetary boundary layer heights (PBLH) for September 02 and 24, 2021, at La Porte. The background shading represents the modeled vertical gradient of potential temperature ($\partial\theta/\partial z$). Red dots indicate

ceilometer-observed PBLH, black line show model-predicted PBLH, and green markers represent the diagnosed residual layer top based on potential temperature gradient analysis.

3.2. Evaluation of residual layer

To quantitatively validate our approach for diagnosing the residual layer, we compared the thermodynamically calculated residual layer heights with observed PBLH data at LaPorte for September 2021, where continuous ceilometer-based observations were available throughout the month. **Figure 4** presents a statistical comparison of how well the WRF base model and our thermodynamic method capture residual layer structures. During nighttime hours (10 PM to 6 AM), the base model significantly underestimates the PBLH and fails to capture the elevated residual layer, as shown in Figure 4ii. In contrast, the thermodynamically diagnosed residual layer heights based on potential temperature gradients show substantially better agreement with observations (Figure 4i), with higher correlation and reduced bias.

To further assess the applicability of our diagnostic approach, we also evaluated the performance during daytime hours (8 AM to 8 PM). Figure 4iii and 4iv compare the thermodynamically calculated PBLH and the model-predicted PBLH, respectively, against observations. Both approaches show better agreement with the observations during the day compared to nighttime, with stronger correlation and lower bias. These results confirm that our method based on vertical gradients of potential temperature effectively captures the residual layer during nighttime conditions, when the WRF base model tends to underestimate boundary layer height, while also performing well for daytime PBLH estimation.

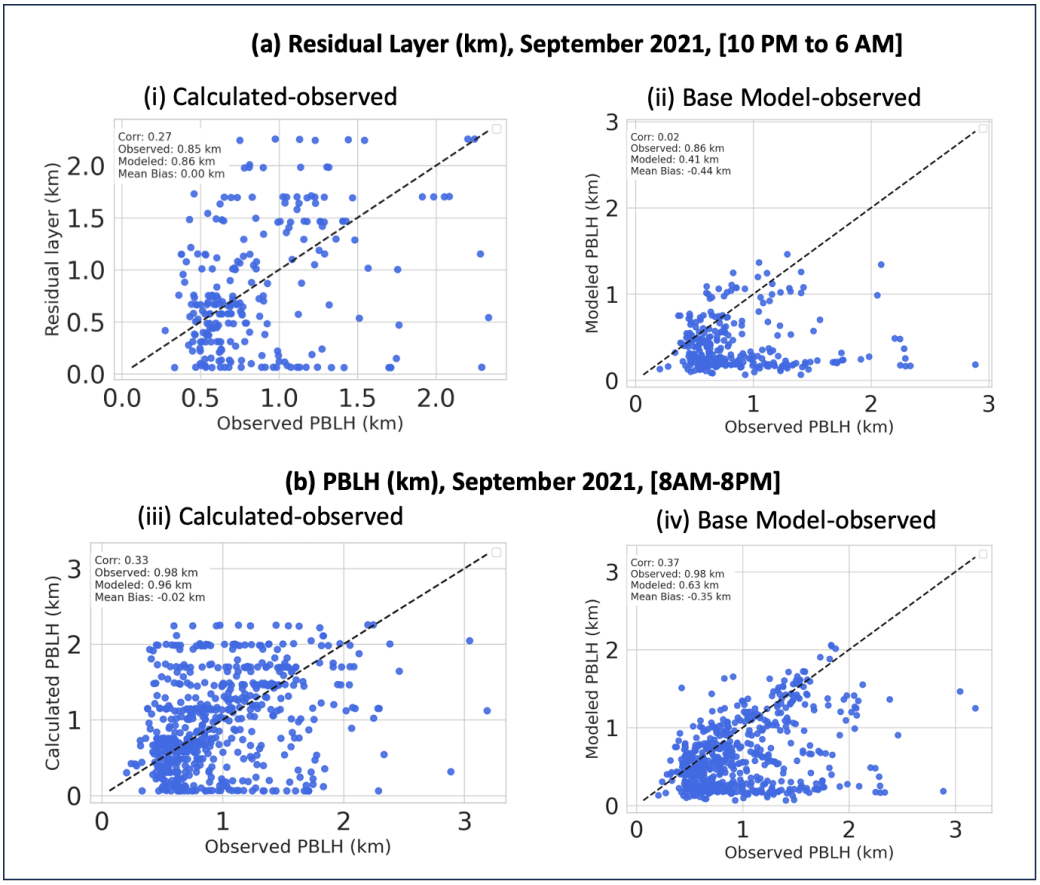

Figure 4 Scatterplots of (i) observed and thermodynamically diagnosed residual layer, (ii) observed and modeled residual layer (km), (iii) observed and thermodynamically calculated PBLH (km) along with (iv) observed-modeled PBLH. The dashed line represents the 1:1 reference line. Statistical metrics such as correlation, mean bias are included in each plot.

4. Sensitivity simulations and residual layer

4.1. Sensitivity simulation results

In Task 4, we identified some perturbations and sensitivity simulations that improved the PBLH over the bay and the Gulf of America and resolved the issues with baseline WRF configurations. We continued our efforts to explore additional parameters and schemes to improve the model simulations of PBLH over water. Throughout this process, we further developed our understanding of the dynamics governing PBLH over water and tested other possible schemes. One additional simulation of notable changes was performed by turning on the 1-D ocean mixed layer model in the WRF and combining this option with one of our previously selected best simulations (PBLH12). There is limited research on the impact of coupling 1-D ocean mixed layer model on PBLH, but coupling is usually preferred to understand air-sea interaction during strong wind conditions. We found coupling the 1-D ocean mixed layer model in WRF shows improved PBLH over water for most of our selected case days. The improvement of PBLH is expected to be the result of improved simulation of the diurnal variation of sea surface temperature (SST)

and the exchange of heat and moisture between the upper ocean and the atmosphere (Zi-Qian & An-Min, 2012). **Table 1** summarizes the previously selected best perturbation runs from Task 4 and the added new simulations in this task.

Table 1 Previously selected best simulations and added additional simulations

Simulation ID	Perturbations
PBL_base	None
PBLH5	C3 = 0.5 (change in closure constant)
PBLH12	New Simplified Arakawa-Schubert (NSAS) cumulus scheme
PBLH14	NSAS + Urban Canopy Model (UCM)
PBLH22	1-D ocean mixed layer model
PBLH23	PBLH12 + PBLH22

We compared the results of the sensitivity simulations (PBLH5, PBLH12, PBLH14, PBLH22, PBLH23) and the base run with the observations using the frequency distribution of daytime (08:00 – 18:00 CDT) of PBLH for all the selected days. The comparison is shown separately for a) the Galveston Bay (Figure 5a) and the Gulf of America (Figure 5b). In the Bay and the Gulf, observed PBLH shows two distinct peaks, the first corresponding to the increased PBLH shortly after sunrise and the second mostly during the afternoon. In all the model experiments, the first peak is skewed towards the higher heights than in the observations, meaning the model persistently overestimates the morning rise of PBLH in the bay. The second peak is of more interest because it predominantly occurs in the afternoon when photochemistry is most active. The base simulation misses this peak by underestimating afternoon PBLH. PBLH12 and PBLH23 more closely replicate the second peak, indicating they improve upon the base simulation by predicting higher afternoon PBLH in the bay that matches better with the observations. Over the Gulf, PBLH23 most closely replicates the first peak. The second peak is also skewed towards the higher heights, indicating improved simulation of PBLH during the afternoon. Further, the spatial plots (Figure 6) help to visualize the change in PBLH throughout the domain.

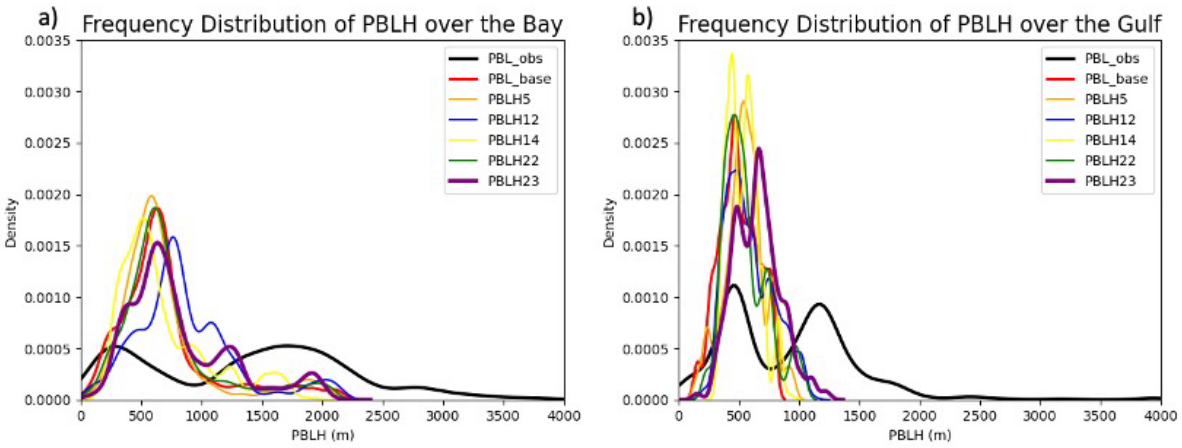

Figure 5 Frequency Distribution of daytime (08:00 -18:00 CDT) planetary boundary layer height (PBLH) from different runs over a) Galveston Bay and b) the Gulf of America for selected days.

Figure 6 shows the spatial variation of the afternoon (12:00 – 16:00 CDT) mean PBLH between Sep 08 and Sep 09 for a) 2021, b) 2022, and c) 2023. The spatial distribution of PBLH across all three years is different, and the effect of perturbation also varies notably in each year for the selected case days. For example, in 2021, the PBLH simulated by the base run (Figure 6a) is higher on both land and water compared to other years. Over the bay, the model slightly underestimates the PBLH from the base and is comparable to the observations (shown by the dots). The influence of perturbation in this year appears to be minimal. On the other hand, in 2022, the PBLH simulated by the base run over both the land and water is lower compared to 2021, and we see a notable improvement in the PBLH due to perturbations PBLH12 and PBLH23 throughout the study domain. Similarly, in 2023 (Figure 6c), PBLH simulated by the base run is very low over land and water. Perturbation simulations increase the PBLH across some portions of land and water. The distinct variation of PBLH and the effect of perturbation across each year prompted us to investigate the cloud characteristics simulated by base and perturbed runs.

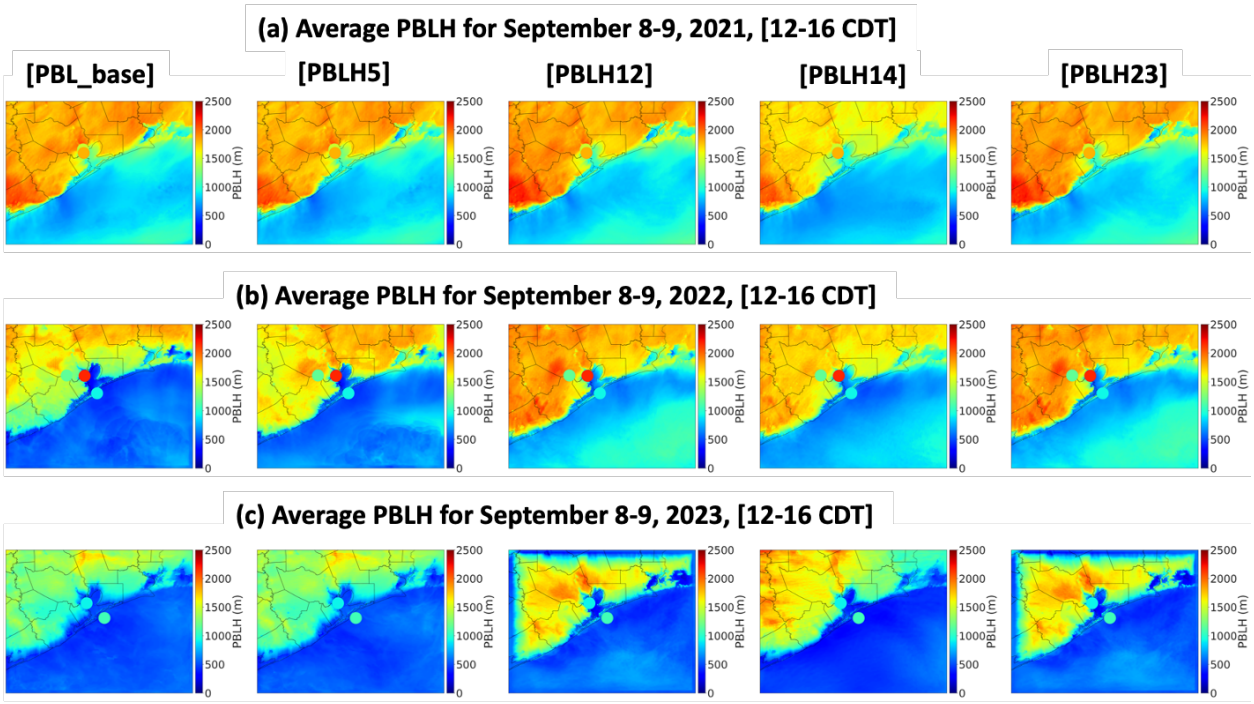

Figure 6 Spatial variation in PBLH (m) from PBL_base, PBLH5, PBLH12, PBLH14, and PBLH23 over the land, Galveston Bay, and Gulf of America for September 08 and 09, (a) 2021, (b) 2022, and (c) 2023. Dot overlaid on the map is the ceilometer observed PBL from LaPorte, University of Houston Pontoon Boat (UHPB), Red Eagle boat (RE), Mobile Air Quality Labs 1 and 2 (MAQL1, MAQL2), and Osprey Boat (OB).

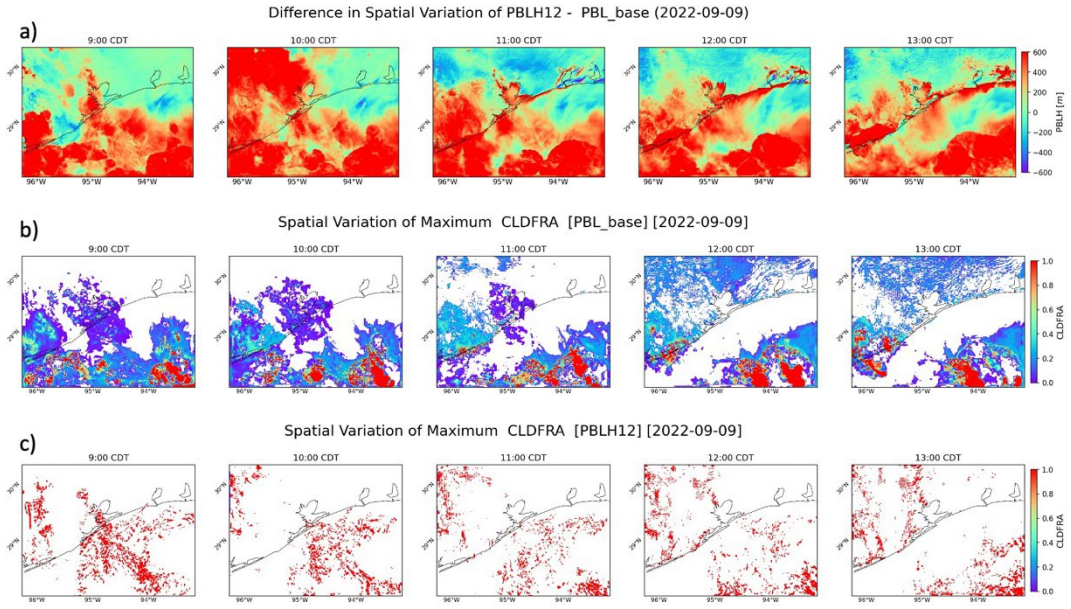

Figure 7 The spatial variation of (a) change in PBLH between PBLH12 and PBLH_base (b) maximum cloud fraction (CLDFRA) simulated by a base run, and (c) maximum cloud fraction simulated by PBLH12 at different hours on September 9, 2022.

Among the selected days in September across all three years, the change in PBLH due to perturbation simulation PBLH12 is notable for the year 2022. To understand the changes caused by the perturbed run (PBLH12), we investigated the cloud-related properties and compared them with the base run. **Figure 7a** shows the change in PBLH between the perturbed run and the base run for Sep 09, 2022, during the hours from 09:00 – 13:00 CDT. Figure 7b and 7c show the maximum cloud fraction simulated by the base run and PBLH12, respectively. The base run simulates the clouds extending over a larger portion of the domain for all the selected hours, whereas the clouds simulated by the perturbed run cover some smaller portions of the domain. The increase in PBLH is higher in the areas where cloud cover is seen in the base run but mostly absent in the perturbed runs. For example, at 11:00 CDT (Figure 7c), the change in PBLH over the bay and the Gulf is higher in the regions where the base run simulates the clouds but is resolved in the perturbed runs. The changes in PBLH are comparatively small when both the perturbed and base run simulate clear skies.

We used the ceilometer's cloud base height (CBH) observations from a mobile boat to see the occurrence of clouds in the observations for the day. **Figure 8** shows the observed CBH along the path of the boat observed at different time hours. While the boat is moving, no CBH observations are seen between the time between 09:00 – 12:00 CDT, meaning the sky is mostly clear along the track of the boat. After 12:00 CDT, clouds are observed at a height of 1.5 to 2 km aloft near the Houston ship channel. The base run simulates the clouds between 09:00 -11:00

CDT along the track of the boat. However, perturbed run PBLH12 shows a clear sky during that time. This shows that the NSAS cumulus adopted in PBHL12 simulated the occurrences of clouds in better agreement with the boat observations along the track than the base simulation.

Upon further investigation, the selected case days in September 2021 were mostly clear in both the base and PBLH12 simulation. The PBLH results from both runs are quite comparable, showing minimal sensitivity to perturbation. In contrast, both the base and PBLH12 simulated thick clouds during Sep 08 and Sep 09, 2023, and improvements were often observed in the regions where PBLH12 simulated fewer clouds compared to the base run. These findings suggest that the PBLH in the model is sensitive to the clouds, and improvements in cloud simulation in the model could better simulate the PBLH over water.

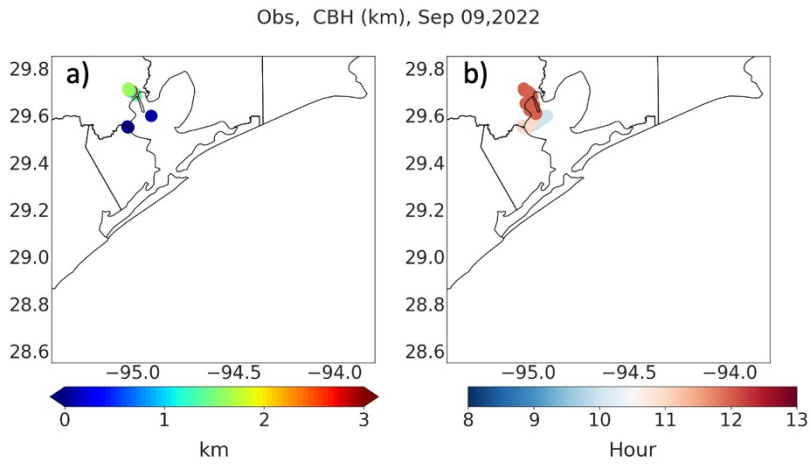

Figure 8 Cloud Base Height (CBH) observed by the mobile boat for Sep 09, 2022, between 08:00 - 11:00 CDT.

4.2. Residual layer

We diagnosed the residual layer height thermodynamically, as described in Section 3.1, using the vertical gradient of potential temperature ($\partial\theta/\partial z$) for selected nighttime periods across 2021, 2022, and 2023. The diagnostic method was applied to the WRF base model (PBL_base) and four selected best perturbation simulations: PBLH5, PBLH12, PBLH14, and PBLH23 to assess how well each configuration represents the spatial structure of the residual layer over land, Galveston Bay, and the Gulf of Mexico.

Figure 9 shows the spatial distribution of thermodynamically diagnosed RL height, calculated from the WRF model potential temperature gradients from midnight to 6 AM for (a) July 27–28, 2021, (b) September 8–9, 2021, (c) September 8–9, 2022, and (d) September 8–9, 2023. RL heights are shown for the WRF base model (PBL_base) and four perturbation simulations: PBLH5, PBLH12, PBLH14, and PBLH23. The ceilometer-observed mean PBLH for the selected time is overlaid as filled circles in all the plots. The circles include the stationary observation

from the LaPorte and mobile observations from UHPB, RE, OB, and MAQL1. Across most days, the diagnosed RL heights from the WRF base and all perturbation simulations show reasonable agreement with observations, with the perturbed simulations showing higher RL over water. However, for September 8–9, 2022, PBLH12, PBLH14, and PBLH23 overestimate the RL height by ~1000 m compared to the observed PBLH from UHPB, RE, and MAQL1, while the base model matched better with the observations.

The thermodynamic approach of calculating RL is empirically developed based on the potential temperature gradient profile from the base run and fine-tuned with the ceilometer observations at LaPorte site for the year 2021.This approach captured the RL height well for the base and the PBLH5 run but the results are not consistent between the perturbation runs PBLH12, PBLH14 and PBLH23. This is probably because the base and PBLH5 use the same cumulus scheme from the base configuration, but other perturbation runs use NSAS cumulus scheme. This suggests that our empirically developed RL diagnosis method needs to be tuned for the NSAS cumulus scheme, which will be conducted in subsequent work of the project.

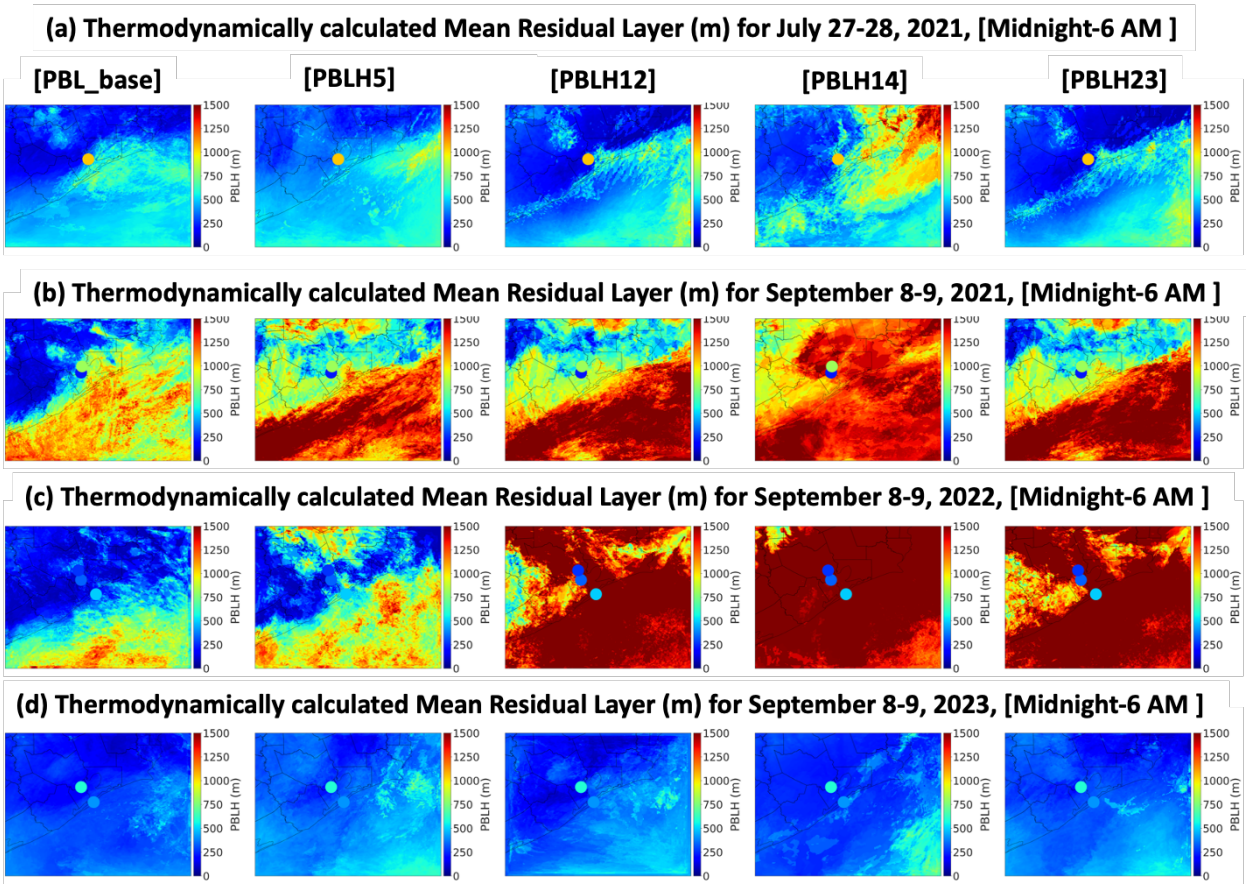

Figure 9 Spatial variation in thermodynamically calculated residual layer from WRF [PBL_base], [PBLH5], [PBLH12], [PBLH14], and [PBLH23] over the land, Galveston Bay, and Gulf of America for (a) July 27-28, 2021, (b) September 8-9 2021, (c) September 8-9 2022, and (d) September 8-9 2023, during the nighttime (Midnight to 6 AM). Dot overlaid on the map is the ceilometer observed mean

PBLH from the LaPorte, University of Houston Pontoon Boat (UHPB), Red Eagle boat (RE), MAQL1, and Osprey Boat (OB).

5. Conclusions

Estimating planetary boundary layer height (PBLH) is important in understanding atmospheric processes, air quality, weather forecasting, and climate modeling. The WRF base model diagnoses only a single PBLH which typically represents the shallow stable boundary layer (SBL) only at night and fails to capture the overlying residual layer (RL). To address this limitation, we developed an empirical method to calculate RL height using vertical gradients of potential temperature ($\partial\theta/\partial z$). The diagnosed RL heights showed a good agreement with the observed PBLH at LaPorte in September 2021, especially at night where the base model fails to capture the layered boundary structures, demonstrating the method's utility. The RL height estimation approach also performed well for daytime PBLH, confirming its broader applicability in capturing layered boundary structures. We applied the RL estimation method across the full model domain for both the WRF base model and the four best-performing perturbation simulations. Comparison with field campaign observations from TAQ1, TAQ2, and TAQ3 shows that the method successfully captured the residual layer structure in both the base simulation and PBLH5 across all eight selected days. PBLH12, PBLH14, and PBLH23 also performed well on most days, with the exception of September 8–9, 2022, where the calculated RL was overestimated. The new PBLH23 simulation performed in this task also improved upon the base model for better PBLH estimation over the water (as with the best cases of PBLH5, PBLH12, PBLH14 simulation identified in Task 4). Overall, our analysis shows that potential temperature gradient-based RL estimation is capable of identifying of RL at night. However, the method is found sensitive to the different cumulus cloud schemes in the model. We will further conduct tuning and calibration for the sensitivity simulations that use the different cloud scheme than the base simulation.

6. Reference

Chen, F., & Dudhia, J. (2001). Coupling an advanced land surface–hydrology model with the Penn State–NCAR MM5 modeling system. Part I: Model implementation and sensitivity. *Monthly Weather Review*, *129*(4), 569–585.

Chen, F., Janjić, Z., & Mitchell, K. (1997). Impact of atmospheric surface-layer parameterizations in the new land-surface scheme of the NCEP mesoscale Eta model. *Boundary-Layer Meteorology*, *85*(3), 391–421.

Iacono, M. J., Delamere, J. S., Mlawer, E. J., Shephard, M. W., Clough, S. A., & Collins, W. D. (2008). Radiative forcing by long-lived greenhouse gases: Calculations with the AER radiative transfer models. *Journal of Geophysical Research: Atmospheres*, *113*(D13).

Liu, X., Wang, Y., Wasti, S., Li, W., Soleimanian, E., Flynn, J., Griggs, T., Alvarez, S., Sullivan, J. T., Roots, M., Twigg, L., Gronoff, G., Berkoff, T., Walter, P., Estes, M., Hair, J. W., Shingler, T., Scarino, A. J., Fenn, M., & Judd, L. (2023). Evaluating WRF-GC v2.0 predictions of boundary layer height and vertical ozone profile during the 2021 TRACER-AQ campaign in Houston, Texas. *Geoscientific Model Development*, *16*(18). https://doi.org/10.5194/gmd-16-5493-2023

Morrison, H., Thompson, G., & Tatarskii, V. (2009). Impact of cloud microphysics on the development of trailing stratiform precipitation in a simulated squall line: Comparison of one-and two-moment schemes. *Monthly Weather Review*, *137*(3), 991–1007.

Nakanishi, M., & Niino, H. (2009). Development of an improved turbulence closure model for the atmospheric boundary layer. *Journal of the Meteorological Society of Japan. Ser. II*, *87*(5), 895–912.

Tiedtke, M. (1989). A comprehensive mass flux scheme for cumulus parameterization in large-scale models. *Monthly Weather Review*, *117*(8), 1779–1800.

Zhang, C., Wang, Y., & Hamilton, K. (2011). Improved representation of boundary layer clouds over the southeast Pacific in ARW-WRF using a modified Tiedtke cumulus parameterization scheme. *Monthly Weather Review*, *139*(11), 3489–3513.

Zi-Qian, W., & An-Min, D. (2012). A New Ocean Mixed-Layer Model Coupled into WRF. *Atmospheric and Oceanic Science Letters*, *5*(3). https://doi.org/10.1080/16742834.2012.11446988